UCSF

UC San Francisco Previously Published Works

Title

Soft X-ray tomography to map and quantify organelle interactions at the mesoscale

Permalink

https://escholarship.org/uc/item/43s5g825

Journal

Structure, 30(4)

ISSN

1359-0278

Authors

Loconte, Valentina
Singla, Jitin
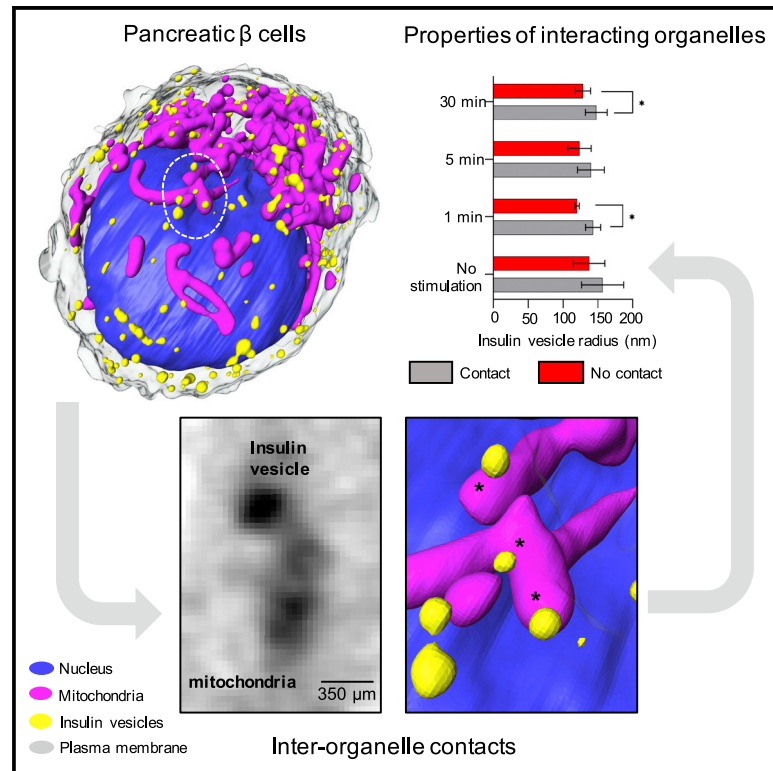Li, Angdi
et al.

Publication Date

2022-04-01

DOI

10.1016/j.str.2022.01.006

Peer reviewed

Structure

Soft X-ray tomography to map and quantify organelle interactions at the mesoscale

Graphical abstract

Authors

Valentina Loconte, Jitin Singla,
Angdi Li, ..., Mark Le Gros,
Kate L. White, Carolyn A. Larabell

Correspondence

carolyn.larabell@ucsf.edu (C.A.L.),
katewhit@usc.edu (K.L.W.)

In brief

Soft X-ray tomography combines rapid collection and high-resolution visualization to understand subcellular reorganization. Loconte et al. use the technique to quantify and describe changes in inter-organelle interactions within pancreatic β cells, providing a unique approach for comprehensive 3D subcellular mapping.

Highlights

- Soft X-ray tomography can be used to quantify intracellular contacts

- Organelles are identified by differential X-ray absorption

- Soft X-ray tomography enables comprehensive subcellular mapping

- Soft X-ray tomography identifies variations in the organelle molecular density

CellPress

Resource

Soft X-ray tomography to map and quantify organelle interactions at the mesoscale

Valentina Loconte,[1,6,7] Jitin Singla,[2,8] Angdi Li,[1] Jian-Hua Chen,[3,4] Axel Ekman,[3,4] Gerry McDermott,[3,4] Andrej Sali,[5] Mark Le Gros,[3,4] Kate L. White,[2,*] and Carolyn A. Larabell[3,4,9,*]

[1]iHuman Institute, School of Life Science and Technology, ShanghaiTech University, Shanghai 201210, China
[2]Department of Chemistry, Bridge Institute, USC Michelson Center for Convergent Bioscience, University of Southern California, Los Angeles, CA 90089, USA
[3]Department of Anatomy, University of California San Francisco, San Francisco, CA 94143, USA
[4]Molecular Biophysics and Integrated Bioimaging Division, Lawrence Berkeley National Laboratory, Berkeley, CA 94720, USA
[5]Department of Bioengineering and Therapeutic Science, Department of Pharmaceutical Chemistry, California Institute of Quantitative Bioscience, University of California San Francisco, San Francisco, CA 94158, USA
[6]Present address: Department of Anatomy, University of California San Francisco, San Francisco, CA 94143, USA
[7]Present address: Molecular Biophysics and Integrated Bioimaging Division, Lawrence Berkeley National Laboratory, Berkeley, CA 94720, USA
[8]Present address: Department of Biosciences and Bioengineering, Indian Institute of Technology Roorkee, Roorkee, Uttarakhand 247667, India
[9]Lead contact
*Correspondence: carolyn.larabell@ucsf.edu (C.A.L.), katewhit@usc.edu (K.L.W.)
https://doi.org/10.1016/j.str.2022.01.006

SUMMARY

Inter-organelle interactions are a vital part of normal cellular function; however, these have proven difficult to quantify due to the range of scales encountered in cell biology and the throughput limitations of traditional imaging approaches. Here, we demonstrate that soft X-ray tomography (SXT) can be used to rapidly map ultrastructural reorganization and inter-organelle interactions in intact cells. SXT takes advantage of the naturally occurring, differential X-ray absorption of the carbon-rich compounds in each organelle. Specifically, we use SXT to map the spatiotemporal evolution of insulin vesicles and their co-localization and interaction with mitochondria in pancreatic β cells during insulin secretion and in response to different stimuli. We quantify changes in the morphology, biochemical composition, and relative position of mitochondria and insulin vesicles. These findings highlight the importance of a comprehensive and unbiased mapping at the mesoscale to characterize cell reorganization that would be difficult to detect with other existing methodologies.

INTRODUCTION

Organelles are traditionally described as intracellular membrane compartments that separate biochemical processes in the cell (Valm et al., 2017; Cohen et al., 2018a). Each compartment is characterized by highly specialized functions that regulate cell homeostasis, division, and response to outside stimuli (Henne, 2021). Their functions are coordinated, and inter-organelle interactions facilitate the communication among different compartments. For example, the juxtaposition between mitochondria and the endoplasmic reticulum (ER) is identified as the locus of lipid biosynthesis (Phillips and Voeltz, 2016); lipids are then transferred from mitochondria to lipid bodies for storage (Valm et al., 2017). Recently, many inter-organelle interactions have been demonstrated to take place at membrane contact sites, where interacting proteins from both organelles regulate the exchange of metabolites between compartments (Scorrano et al., 2019). For example, mitochondria-associated membranes are regions of the ER that reversibly tether to mitochondria; deter-

mining their connectivity (i.e., contact numbers and localization) and temporal reorganization informs about cell calcium and lipid homeostasis (Vance, 2014). High-resolution imaging techniques provide an accurate identification of organelle interactions (Scorrano et al., 2019), and three-dimensional (3D) maps of entire cells are required to characterize the frequency of the interactions, to identify the number and location of inter-organelle contacts, and to determine whether they are altered during specific pathological conditions (Díaz et al., 2021).

Fluorescence microscopy largely contributed to the discovery of extensive communication between organelles. The rise of selective and synthetic fluorescence probes, together with the advancements in biotechnological methodologies, facilitated the discovery of subcellular mechanisms, such as the description of the role of the ER in mitochondrial fission and fusion (Cohen et al., 2018b; Guo et al., 2018; Valm et al., 2017). Similarly, transmission electron microscopy (TEM) (Graham et al., 2019) and focused-ion-beam-scanning electron microscopy (FIB-SEM) (Kizilyaprak et al., 2013; Kremer et al., 2015) have provided

exquisite details of the 3D architecture of the cell at extremely high resolutions, unraveling mechanisms related to the interaction between subcellular compartments and/or cytoskeleton (Müller et al., 2020). However, due to the limited penetration of the electron beam and specimen thickness, electron microscopy requires the samples to be fixed, stained, dehydrated, embedded in plastic, and sectioned (Noske et al., 2008). Cryo-electron tomography (cryo-ET) can image 200-nm-thick sections of adherent cells in a near-native state with a resolution on the order of 30 Å (Lučić et al., 2013; Mahamid et al., 2016). However, due to the high magnification of the technique and the low penetration of the electron beam, the field of view is limited to a few hundred nanometers (Buckley et al., 2020). Moreover, scattering of the incident electron beam decreases the signal-to-noise ratio of the collected micrographs (Peet et al., 2019). Alternatively, imaging biological samples using soft X-ray tomography (SXT) enables imaging intact cells (Larabell and Nugent, 2010) with a spatial resolution of 35–60 nm (McDermott et al., 2012; Schneider et al., 2010) within the mesoscale size range, from 1–20 μm (Le Gros et al., 2012). Cells are imaged in the "water window" (284–583 eV photon energy), where the soft X-ray beam is attenuated almost entirely by bioorganic material. The density of the organic compounds in each voxel is quantified by measuring the X-ray attenuation (known as the linear absorption coefficient-LAC), and its quantification adheres to the Beer-Lambert's law (Do et al., 2015; Ekman et al., 2017). Because each organelle has a distinct concentration of carbon-rich organic molecules, the LAC values can be used as a hallmark to identify individual cell substructures. SXT leverages the natural contrast of cells and does not require imaging probes or fluorescent dyes (Attwood, 2000). Compared with other 3D imaging approaches, SXT is a high-throughput technology with a data collection time of approximately 10 min (Parkinson et al., 2012), which allows for the comparison of larger numbers of cells under multiple biological conditions.

In this work, we demonstrate the unique quantitative abilities of SXT. Our goal was to develop a more in-depth data analysis pipeline for mapping and quantifying inter-organelle interactions with SXT using their natural contrast rather than stains. To do so, we build upon our initial observation of insulin vesicle-mitochondria contacts in pancreatic β cells (White et al., 2020). We analyzed new datasets to explore interactions between insulin vesicles and mitochondria, adding a detailed analysis of the ultrastructural reorganization that occurs during a very early stage of the secretory process (~1 min) and a comparison with later time points. In pancreatic β cells, mitochondria are involved in several mechanisms intended for the production and secretion of insulin. For example, ATP production triggers insulin secretion by closing the ATP-dependent potassium channels (Rorsman et al., 2000). Additionally, there is an association between mitochondrial metabolic products (i.e., Ca^{2+}, NADH, pyruvate, and glutamate) and the activation of the ATP-independent insulin secretory pathways (Maechler et al., 2006; Wiederkehr and Wollheim, 2006). The interactions between insulin vesicles and mitochondria were examined previously (Maechler and Wollheim, 2001; Wollheim, 2000) but never mapped in whole cells.

To demonstrate the capability of SXT to map and quantify interactions between organelles, we examined the co-localization of insulin vesicles and mitochondria. We tracked these organelle interactions after stimulation with glucose and exendin-4, which is an incretin analog of the glucagon-like protein one receptor (GLP1R) agonist that potentiates the glucose effect on insulin stimulation (Eng et al., 1992; Gedulin et al., 2005; Kolterman et al., 2003). We captured organelle reorganization as a response to different types of stimulation and tracked alterations of mitochondria-vesicle interactions during the first and second phases of insulin secretion. We characterized the interactions that occur during the secretory process and evaluated the randomness of the interactions and drug stimulation on organelle association. Finally, we showed that vesicles in contact with the mitochondria network have similar LAC values, but different sizes, compared with vesicles farther from mitochondria.

RESULTS

INS-1E architecture by SXT

We used SXT to investigate alterations in cell morphology and molecular density of INS-1E rat insulinoma cells at three different time points representing the early stage of the biphasic secretory process (1 min), the late stage of the first phase of secretion (5 min), and the early stage of the second phase of secretion (30 min) compared with unstimulated cells. Four experimental conditions were examined: no treatment, high glucose (25 mM), high glucose in combination with exendin-4 (Ex-4), and Ex-4 alone. This last condition was used as a control to verify the recapitulation of the features observed with co-stimulation with high glucose. The analysis was performed on 56 cells in total. The collective results in Table 1, though not all statistically significant, represent the type of large datasets that SXT can generate, providing an informative and in-depth resource for exploring cellular structure.

Experimental manipulations were conducted using INS-1E cells in suspension. White et al. previously showed that there is no significant difference in the amount of insulin secretion between cells in suspension and adherent cells (White et al., 2020). In addition, the organization of the readily releasable and reserve pools is conserved (Bratanova-Tochkova et al., 2002). After manipulation, cells were placed in thin-walled glass capillaries, frozen, and imaged with SXT. The cells measured between 10–12 μm, which is easily penetrated by the soft X-ray beam (Duke et al., 2014). With a field of view of 16 μm × 16 μm at 60-nm spatial resolution (Weinhardt et al., 2020), the whole-cell architecture can be collected in one single data acquisition. Data collection was performed by rotating the cells through 180° to ensure a near-isotropic reconstruction (Figure 1A); this eliminates the loss of information caused by the "missing wedge" that is inherent to imaging cells grown on flat specimen mounts (Groen et al., 2019; Loconte et al., 2021).

SXT generates 3D images of whole cells and subcellular organelles (Figure 1B), which makes it possible to determine the volumes of cells and organelles. We show that there was a broad range in cell size; the total volume of untreated INS-1E cells was 715 ± 148 μm³ (Figure 1C; Table 1). To identify, label, and characterize specific organelles, we used a combination of LAC values and 3D morphology. We demarcated the cell nucleus by tracing the nuclear surface (Le Gros et al., 2016). The volume of the nucleus was 199 ± 32 μm³, comprising an average of 30.7% ± 3.4% of the total cell volume; the average LAC value

Table 1. Quantitative analysis of the segmented organelles

|		25-mM glucose			25-mM glucose +10 nM Ex-4			10-nM Ex-4	
Stimulation	0 min (n = 8)	1 min (n = 4)	5 min (n = 8)	30 min (n = 8)	1 min (n = 4)	5 min (n = 8)	30 min (n = 8)	5 min (n = 4)	30 min (n = 4)
Cell volume (μm^3)	715 ± 148	636 ± 137	752 ± 125	873 ± 261	633 ± 138	1,224 ± 304	733 ± 246	1,040 ± 232	801 ± 157
Nucleus volume (μm^3)	199 ± 32	180 ± 31	238 ± 51	228 ± 61	196 ± 27	397 ± 97	203 ± 74	334 ± 38	300 ± 65
Nucleus volume (%)	28 ± 4	31 ± 23	32 ± 5	27 ± 38	29 ± 3	33 ± 2	28 ± 5	33 ± 5	37 ± 4
Nucleus LAC (μm^{-1})	0.24 ± 0.01	0.27 ± 0.02	0.28 ± 0.02	0.25 ± 0.02	0.29 ± 0.02	0.26 ± 0.02	0.27 ± 0.02	0.26 ± 0.02	0.24 ± 0.02
Mitochondria volume (μm^3)	32 ± 11	42 ± 3	43 ± 10	38 ± 12	51 ± 9	73 ± 15	41 ± 7	86 ± 37	60 ± 21
Mitochondria volume (%)	4.4 ± 0.9	6.8 ± 0.9	5.8 ± 1.4	4.5 ± 1.3	8.2 ± 1.3	6.4 ± 0.9	5.9 ± 1.3	8.5 ± 3.4	7.5 ± 2.0
Mitochondria LAC (μm^{-1})	0.32 ± 0.02	0.35 ± 0.03	0.36 ± 0.02	0.32 ± 0.03	0.36 ± 0.02	0.33 ± 0.02	0.35 ± 0.03	0.32 ± 0.03	0.30 ± 0.03
Cytosol volume (μm^3)	516 ± 130	441 ± 110	514 ± 96	644 ± 205	453 ± 113	827 ± 210	530 ± 181	706 ± 197	501 ± 103
Cytosol volume (%)	72 ± 4	69 ± 2	68 ± 5	72 ± 5	71 ± 3	68 ± 2	74 ± 3	67 ± 5	63 ± 4
Cytosol LAC (μm^{-1})	0.25 ± 0.01	0.28 ± 0.02	0.29 ± 0.02	0.28 ± 0.01	0.28 ± 0.03	0.27 ± 0.03	0.28 ± 0.03	0.26 ± 0.01	0.25 ± 0.02
Insulin vesicle total number	319 ± 93	310 ± 13	409 ± 139	787 ± 204	380 ± 106	386 ± 186	515 ± 156	280 ± 140	244 ± 97
Insulin vesicle total volume (μm^3)	4.0 ± 1.9	3.1 ± 1.3	4.0 ± 2.6	7.5 ± 2.3	3.2 ± 0.8	3.8 ± 2.0	5.4 ± 2.8	4.7 ± 3.9	2.1 ± 0.9
Insulin vesicle total volume (%)	0.56 ± 0.28	0.48 ± 0.14	0.55 ± 0.41	0.89 ± 0.30	0.55 ± 0.26	0.31 ± 0.14	0.73 ± 0.32	0.43 ± 0.36	0.29 ± 0.15
Insulin vesicle LAC (μm^{-1})	0.37 ± 0.03	0.42 ± 0.02	0.46 ± 0.03	0.40 ± 0.02	0.44 ± 0.04	0.45 ± 0.03	0.43 ± 0.03	0.44 ± 0.02	0.43 ± 0.04
Mitochondria-connected insulin vesicles (%)	9.7 ± 6.1	14.7 ± 6.2	21.1 ± 9.8	10.3 ± 2.9	23.8 ± 15.7	20.1 ± 11.7	15.3 ± 5.7	16.9 ± 8.9	28.8 ± 10.1

List of volume and LAC values of cells, nuclei, mitochondria, cytosol, and insulin vesicles for each condition and time point. The mean numbers of insulin vesicles per condition and the percentage of vesicles in contact with mitochondria are also reported. Each value is reported with its standard deviation.

was 0.26 ± 0.02 μm^{-1}. In the cytoplasm, we segmented the mitochondrial network and insulin vesicles (Figure 1B). Mitochondria, identified by their characteristic elongated shape, had an average LAC value of 0.32 ± 0.02 μm^{-1}, accounting for 4.37% ± 0.86% of the whole-cell volume in unstimulated cells. The spherical insulin vesicles had an average LAC value of 0.37 ± 0.03 μm^{-1} and occupied just 0.56% ± 0.28% of the total volume of unstimulated cells (Table 1).

Organelle properties and spatial distribution
We first calculated the total volume of cells and organelles after stimulation with glucose alone or with Ex-4 at the three different time points (Figure 1C; Table 1). Glucose alone did not trigger any significant changes in the total volume of the cell, nucleus, or mitochondria after 1, 5, or 30 min; there was, however, a small but statistically significant increase in total insulin vesicle volume (from 4.0 ± 0.1.9 to 7.5 ± 2.3 μm^3) after 30 min. After 5-min stimulation with glucose + Ex-4, however, there was an increase in total cell volume (from 715 ± 148 to 1,224 ± 304 μm^3), which was accompanied by an increase in total nuclear volume (from 199 ± 32 to 397 ± 97 μm^3) and total mitochondria volume (from 32 ± 11 to 73 ± 15 μm^3). In cells treated with Ex-4 alone for 5 min, there was a statistically significant increase in total nuclear volume (from 199 ± 32 to 334 ± 38 μm^3) and total mitochondrial volume (from 32 ± 11 to 86 ± 37 μm^3) and an increase in total mitochondrial volume to 60 ± 21 μm^3 after a 30-min treatment with Ex-4 alone (Figure 1C; Table 1).

Given the heterogeneity seen in cultured cell lines, and the large variance in cell size, we analyzed changes in the volume of mitochondria and insulin vesicles normalized by cell volume. We observed an increase in the percent volume of mitochondria after 1 min of stimulation with high glucose, both without (6.76% ± 0.93%) and with (8.18% ± 1.25%) Ex-4, compared with unstimulated cells (4.37% ± 0.86%). Mitochondrial volume began to decrease after 5 min of stimulation under both conditions, although more slowly in cells stimulated with glucose + Ex-4 (Figure 2A), suggesting that there is an effect of Ex-4 on mitochondria biogenesis (Kang et al., 2015). SXT also provides quantitative information about the density of the biomolecules present in a subcellular structure and a specific LAC value for that organelle. The range of LAC values in mitochondria of untreated INS1E cells (0.32 ± 0.02 μm^{-1}) was consistent with values we previously reported for other mammalian cells (https://ncxt.org/primer/). To determine whether the general biochemical composition of mitochondria was affected by each of the treatments, we calculated the average LAC values after treatment. As reported in Table 1 and Figure 2B, no significant changes were visible after treatment with glucose + Ex-4 at any time point compared with the unstimulated cells. After 5 min of stimulation with high glucose, however, the mitochondrial LAC value was significantly increased (0.36 ± 0.02 μm^{-1}) compared with both unstimulated (0.32 ± 0.02 μm^{-1}) and glucose- + Ex-4-stimulated cells (0.33 ± 0.02 μm^{-1}) within the same time point. This indicates that there was an increase in
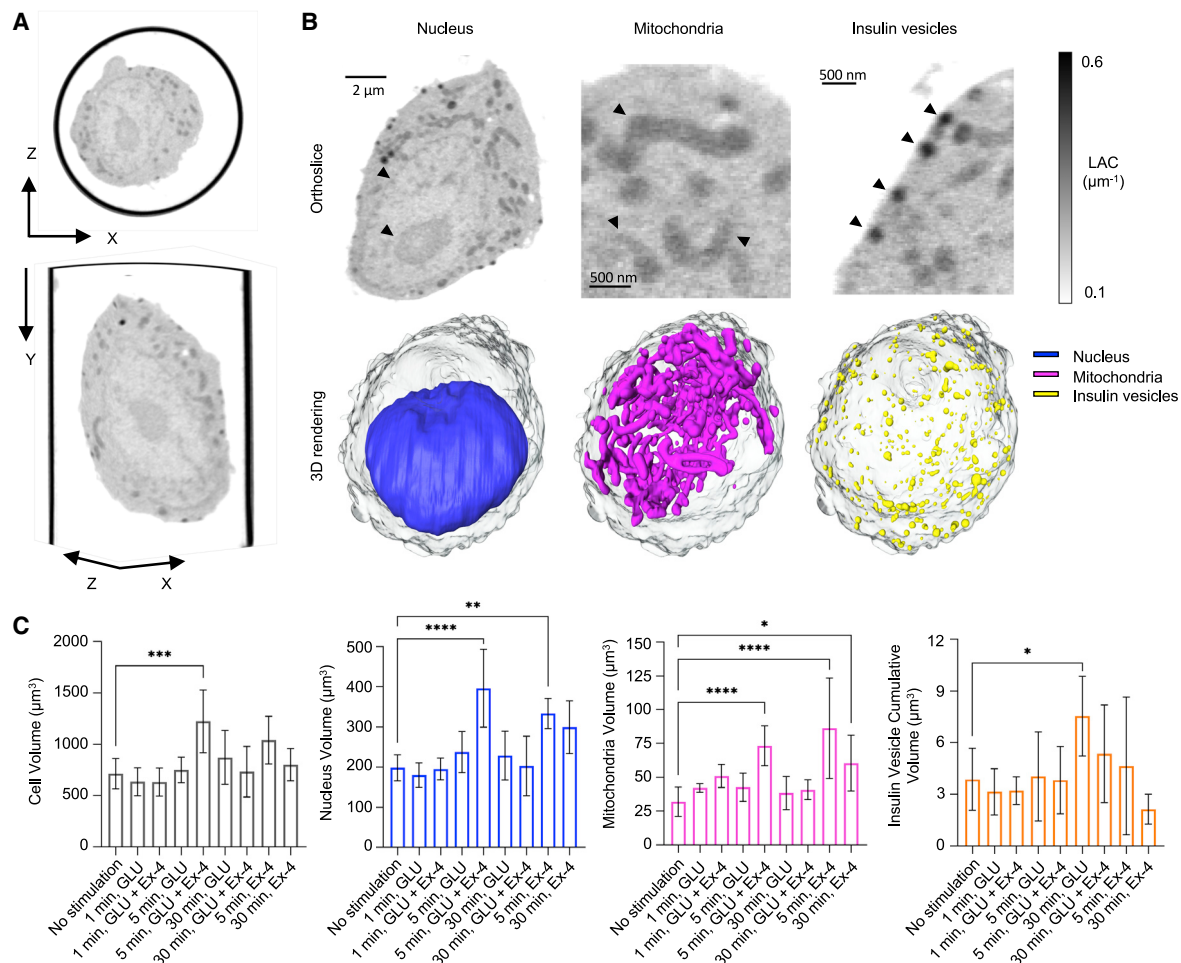
Figure 1. Isotropic reconstruction of a single pancreatic β cell

(A) The whole-cell volume is shown in the XY (bottom) and XZ (top) planes.

(B) Organelles are defined based on different levels of gray values, with a threshold between 0.1–0.6 μm⁻¹. Single orthoslices (top) and relative 3D rendering (bottom) represent a single β cell after 1 min of high glucose treatment (cell ID: 821_12). In detail, the rendering shows: nucleus (blue), mitochondrial network (magenta), and insulin vesicles (yellow) and their spatial distribution. All organelles in the orthoslices are highlighted by an arrowhead, with 2 μm and 500 nm scale bar for nucleus, and mitochondria and insulin vesicles,respectively.

(C) Plots representing the overall volume of the organelle in the cells per condition and time point. We report alterations in the total volume of each type of organelles in the following order: from left, changes in cell volume with a signific difference between 5-min-stimulated cells with high glucose + Ex-4 and unstimulated cells (***p = 0.0002); changes in the nucleus volume with a significant difference between unstimulated cells and 5-min-stimulated cells with high glucose + Ex-4 (****p < 0.0001) and 5-min-stimulated cells with 10 nM Ex-4 (**p = 0.0058); changes in the volume of the mitochondrial network with significant difference between unstimulated cells and 5-min-stimulated cells with high glucose + Ex-4 (****p < 0.0001), 5-min-stimulated cells with Ex-4 (****p < 0.0001), and 30-min-stimulated cells with Ex-4 (*p = 0.0189); and finally, changes in the insulin vesicle cumulative volume with significant difference between unstimulated cells and 30-min-stimulated cell with high glucose (*p = 0.0170). Statical significance was validated using Dunnett's multiple comparison test. Error bars represent standard deviations (SDs).

the concentration of carbon-rich components (i.e., proteins, lipids, and metabolites) per voxel in mitochondria after 5-min stimulation with glucose (Figure 2B).

To identify and track the proximity between mitochondria and insulin vesicles under all conditions, we generated a 3D map of the segmented organelles (Figure 2C). We then calculated the minimal distances between vesicle centers and surfaces of the most proximal branch of the mitochondrial network and quantified the average distances. We found that the mean vesicle-mitochondrial distance decreased after stimulating the cells with high glucose + Ex-4. This was observed throughout the cells

and is statistically significant after 5 and 30 min of stimulation compared with unstimulated cells, indicating a tighter association between the mitochondria and insulin vesicles under these conditions (Figure 2C).

We then compared the number of insulin vesicles seen during the first minute of secretion with the later stages of the insulin secretory process (Figure 3A; Table 1). There was no significant change in the number of insulin vesicles at 1-min post stimulation with either glucose alone or in the presence of Ex-4. At 30-min post stimulation, there was a significant increase after stimulation with glucose alone (787 ± 204) and with glucose + Ex-4

CellPress
OPEN ACCESS
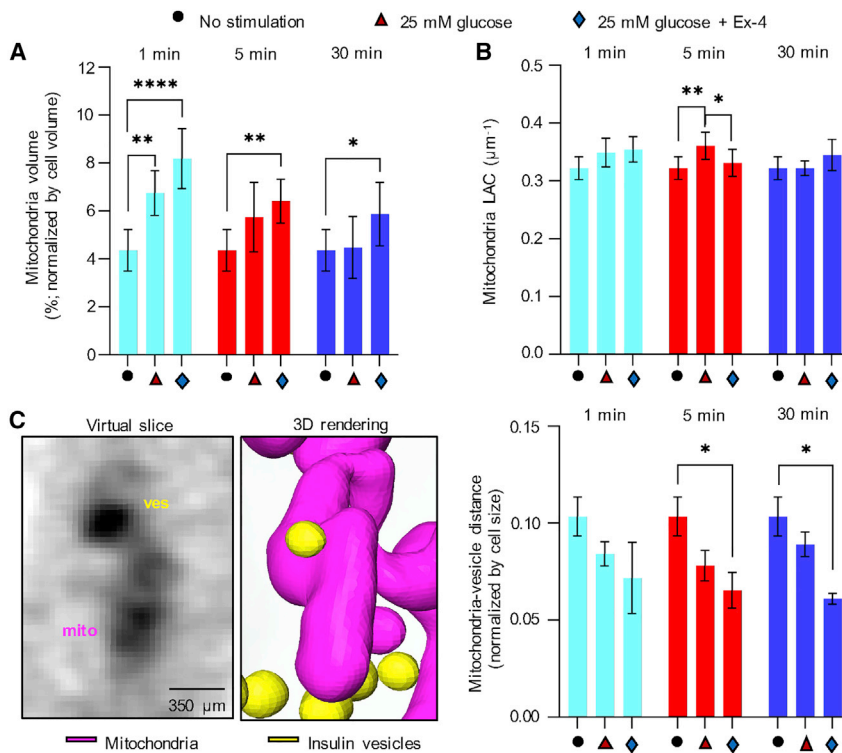
Figure 2. Effect of glucose and Ex-4 stimulation on mitochondria properties and spatial distribution

(A) Percentage of cell volume occupied by mitochondria for each condition and time point. Compared with unstimulated cells, a significant difference is observed after 1 (****p < 0.001 and **p = 0.042), 5 (**p = 0.0035), and 30 (*p = 0.0460) min of stimulation with high glucose ± Ex-4 (Tukey's multiple comparison test).

(B) Mean mitochondria LAC value. A significant difference is observed between unstimulated cells and cells stimulated with 25 mM glucose for 5 min (**p = 0.0071) and between 25-mM-glucose- versus 25-mM-glucose+10-nM-Ex-4-stimulated cells for 5 min (*p = 0.0426). Statistical significance was evaluated using Tukey's multiple comparison test.

(C) Left: an orthoslice and 3D rendering of interacting insulin vesicles and mitochondria after 1 min of stimulation with high glucose (scale bar: 350 nm). Right: mean distance between insulin vesicles and mitochondria normalized by cell size shows a significant decrease in the distance between unstimulated and glucose- + Ex-4-stimulated cells after 5 and 30 min (*p = 0.0269 and *p = 0.0121, respectively; Tukey's multiple comparison test). Error bars represent SDs.

(515 ± 156) compared with the number in unstimulated cells (319 ± 93). At both 5- and 30-min post stimulation, there were significantly fewer vesicles after stimulation with glucose + Ex-4 than with glucose alone, suggesting that Ex-4 may alter the rate of insulin secretion during the second phase of secretion, as reported in White et al. (2020), but does not affect the first phase.

There was a significant increase in the molecular density (LAC value) of the vesicles stimulated with glucose and glucose + Ex-4 compared with unstimulated cells; the LAC values after 5-min glucose (0.46 ± 0.02 μm^{-1}) and glucose + Ex-4 (0.45 ± 0.04 μm^{-1}) stimulation are significantly higher than untreated cells (0.37 ± 0.03 μm^{-1}) (Figure 3B; Table 1). These data suggest that there has been an alteration in vesicle maturation at the end of the first phase of secretion. Finally, measuring the distance of vesicles from the plasma membrane (PM) shows that there is a decrease in the number of vesicles just beneath the PM (within 0.0–0.1; Figure 3C) after 1- and 5-min stimulation with glucose + Ex-4, and after 5-min stimulation with glucose alone, indicating a faster deployment to secretion of the vesicle population during the first phase of secretion (Figure 3C). At the same time, there was an increase in the number of vesicles seen slightly farther from the PM (0.2–0.4) at 1 min after glucose + Ex-4 stimulation, and even deeper after 5-min glucose with and without Ex-4, indicating a repopulation of the reserve pools (Rorsman et al., 2000).

Dynamics of mitochondria-vesicle interactions during insulin secretion

To investigate the frequency of the interaction between insulin vesicles and mitochondria, we quantified the number of mitochondria-vesicle contacts per cytosolic volume. We observed a statistically significant increase in mitochondria-vesicle con-

tacts after 5-min treatment with high glucose without Ex-4 (Figure 4A, left panel) and after 1-min treatment with Ex-4 (Figure 4A, right panel) compared with unstimulated cells. We also analyzed the distribution of contacts with respect to the PM (Figure 4B) and found that there is an increase in contacts near the PM after 1-min treatment with high glucose ± Ex-4. This was confirmed by determining the average distance of the contacts from the PM. The shortest distance of mitochondria-vesicle contact from the PM occurs after 1- and 30-min stimulations with high glucose ± Ex-4 (Figure 4C). Interestingly, the contacts at 5 min cover a broad region beneath the PM after the stimulation with glucose + Ex-4, suggesting that this interaction in the cell might play a role in the active vesicle movement toward the PM and in vesicle maturation.

Given the simultaneous increase in the mitochondria volume in cells treated with Ex-4 and the number of insulin vesicles after 30 min of stimulation with glucose ± Ex-4, we aimed to evaluate the randomness of the interaction accounting for the crowdedness of the cell. We defined a congestion index (C.I., see STAR Methods) and correlated its value to the fraction of insulin vesicles associated with mitochondria for each cell. Figure 5A shows that unstimulated cells and those stimulated with glucose for 30 min cluster at regions with a lower C.I. (black circle = below 0.08), with contacts between 3% and 13% of the total number of vesicles. On the other hand, those cells treated with glucose + Ex-4 for 1 and 5 min were randomly distributed in the higher C.I. range (greater than 0.08), with contacts between 4% and 25% of the vesicles in contact with mitochondria. There is a high degree of randomness in the populations of cells treated with glucose ± Ex-4 for 1 and 5 min (Figures 5A–5C), highlighting cell-dependent variability in vesicle-mitochondria interactions and cell-to-cell

A

B

C

Distance from PM (normalized by cell size)
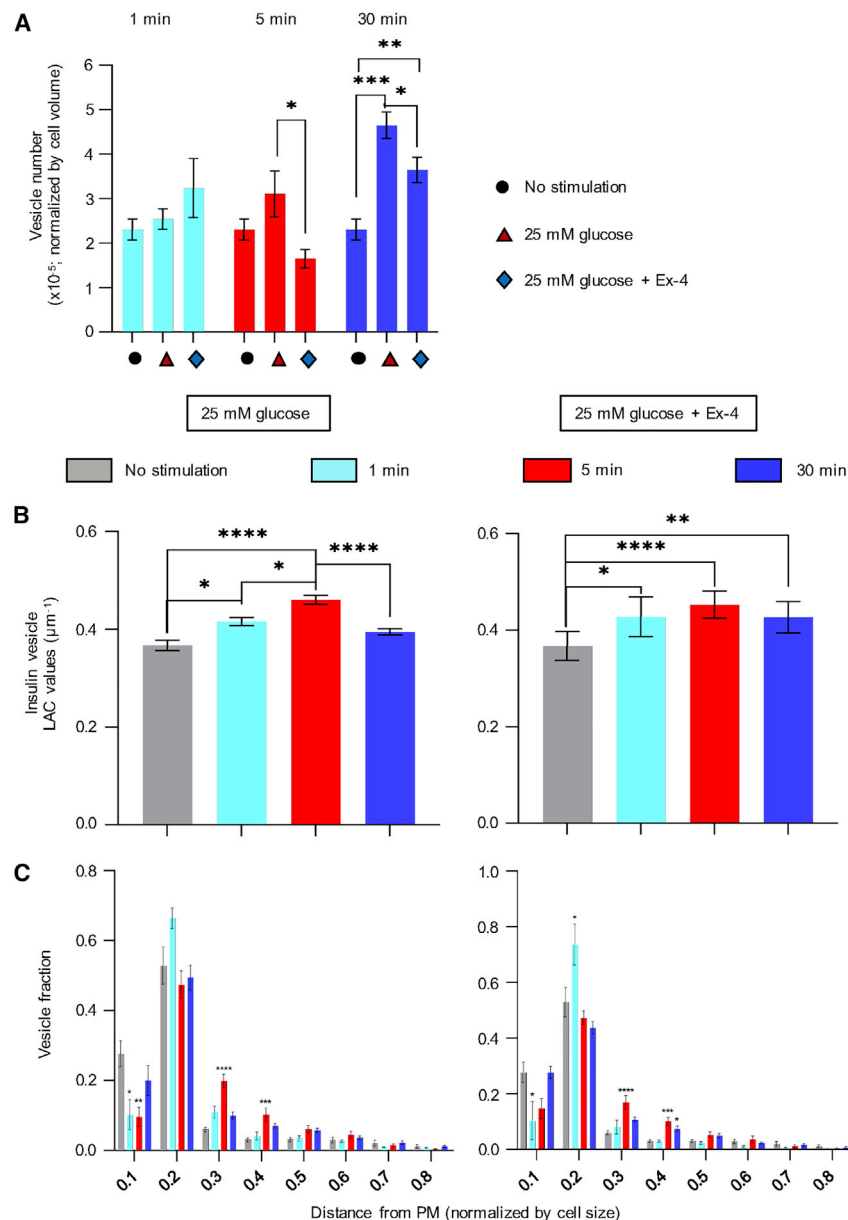
Figure 3. Effect of the high glucose stimulation with and without Ex-4 on insulin vesicle properties and spatial distribution

(A) Number of insulin vesicles during the two phases of insulin secretion. There was no significant change in the number of vesicles after 1-min stimulation with glucose alone or in the presence of Ex-4. A significant increase in vesicle numbers was seen at 30-min post stimulation with glucose alone (787 ± 204, ****p < 0.0001) and with glucose + Ex-4 (515 ± 156, **p = 0.0062) compared with unstimulated cells (319 ± 93). Fewer vesicles were seen after stimulation with glucose + Ex-4 at both 5 (*p = 0.0191) and 30 (*p = 0.0436) min than when stimulated by glucose alone.

(B) Mean vesicle LAC values. Left: treatment with 25-mM glucose. Insulin vesicle LAC values steadily increase after 1-min stimulation from 0.37 ± 0.03 to 0.42 ± 0.02 μm^{-1} (*p = 0.0138) and to 0.46 ± 0.02 μm^{-1} after 5-min stimulation (****p < 0.0001); there is also a significant difference in the increase between 1- and 5-min stimulation (*p = 0.264). At 30-min post stimulation with glucose, there is a significant decrease in LAC value to 0.40 ± 0.02 μm^{-1} compared with the LAC seen at 5-min post stimulation (****p < 0.0001). Right: treatment with 25-mM glucose + Ex-4. An increase in LAC values after stimulation is seen after 1-min glucose + Ex-4 to 0.44 ± 0.04 μm^{-1} (*p = 0.0226), at 5 min to 0.45 ± 0.03 μm^{-1} (****p < 0.0001), and at 30 min to 0.43 ± 0.03 μm^{-1} (**p = 0.0051) (Tukey's multiple comparison test).

(C) Plots representing the position of vesicles in the cell as normalized distance from the PM (0.0 is the closest distance to PM and 1.0 the farthest). With respect to the unstimulated cells, significant differences in vesicle population are found for 25-mM glucose-stimulated cells (left panel) within 0.1 from the PM (1-min stimulation: *p = 0.0316; 5-min stimulation: **p = 0.0040), 0.2–0.3 (5-min stimulation: ****p < 0.0001), and 0.3–0.4 (5-min stimulation: ***p = 0.005); the same analysis is performed for 25-mM glucose- + Ex-4-stimulated cells (right panel), with differences within 0.1 from the PM (1-min-stimulated cells: *p = 0.0337), 0.1–0.2 (1 min: *p = 0.0129), 0.2–0.3 (5-min-stimulated cells: ****p < 0.0001), 0.3–0.4 (5 min: ***p = 0.006 and *p = 0.0488) (Dunnett's multiple comparison test). In all panels, error bars represent SDs.

variability (White et al., 2020). Moreover, given the high variability of total cell volume among conditions and time points, the C.I. does not carry the accuracy required to determine the randomness of the interaction.

To explore whether vesicle-mitochondria contacts are caused by crowdedness rather than biological function, we compared the properties of the vesicles associated with mitochondria with the vesicles farther away (Figures 5D–5E). The vesicles in contact with the mitochondria did not show a significantly higher mean LAC value after the treatment with glucose and glucose + Ex-4 (Figure 5D). We did, however, observe an increase in the mean radius of the vesicles associated with mitochondria compared with vesicles that are not associated with mitochondria after treatment with glucose for 1 min (143 ± 11 nm, contacts; 120 ± 3.0 nm, no contacts) and 30 min (148 ± 16 nm, con-

tacts; 129 ± 11 nm, no contacts). An increase in contacts was also seen after 30-min treatment with glucose + Ex-4 (155 ± 23 nm, contacts; 127 ± 21 nm, no contacts) (Figure 5E). The significant difference in the physical properties seen between those vesicles associated with mitochondria and those not associated with mitochondria suggests that the interactions may be of biological significance, potentially contributing to the vesicle maturation process.

Quantification of the Ex-4 effect on the contact spatial distribution and organelle properties

It has been reported that Ex-4 enhances mitochondrial biogenesis and increases cell mass and function by restoring insulin secretion (Kalavalapalli et al., 2019; Kang et al., 2015). The role of Ex-4 has been explored primarily in combination with
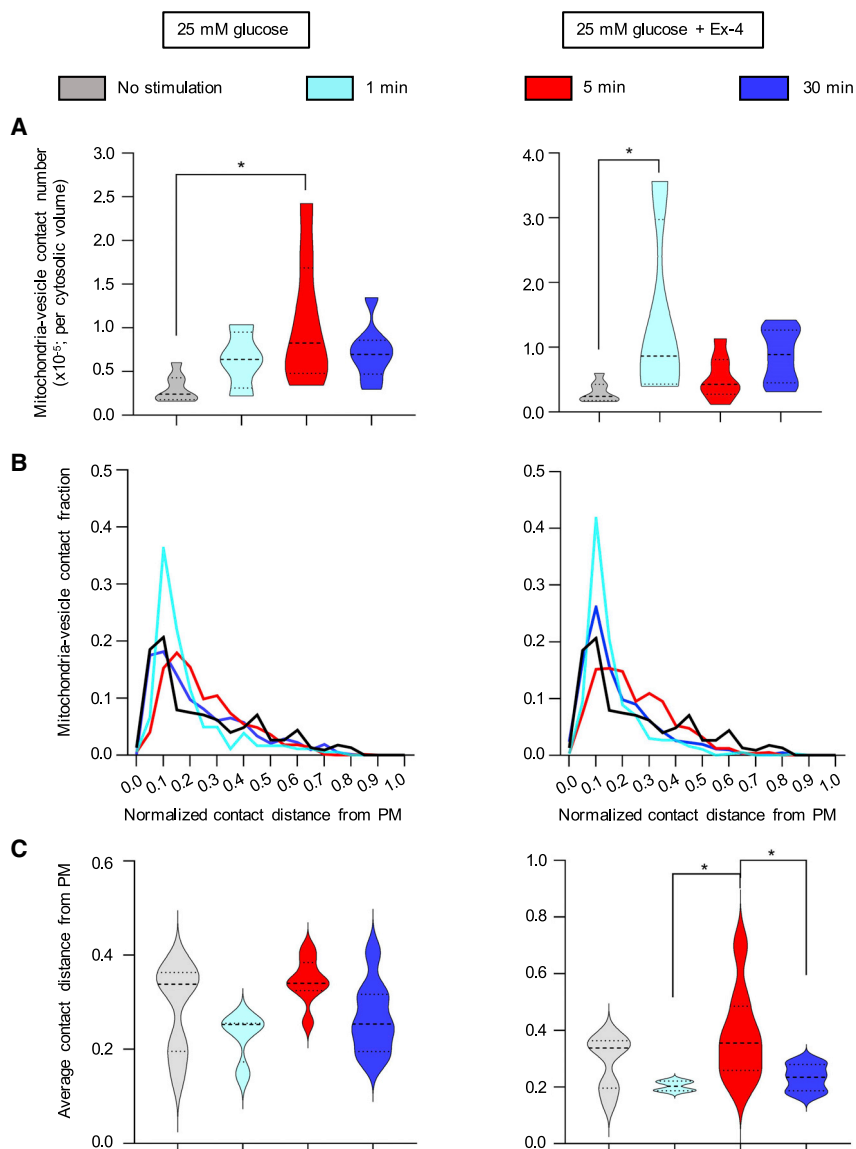
Figure 4. Quantification of the spatial distribution of mitochondria-insulin vesicle contacts and localization with respect to PM

(A) Comparison of the number of mitochondria-insulin vesicle contacts per cell normalized by cytosolic volume. The mean value of contacts at each time shows a significant difference between unstimulated and 5-min-stimulated cells with high glucose (*p = 0.0126) (left panel) and 1-min-stimulated cells with 25-mM glucose + Ex-4 (*p = 0.0267) (right panel) (Tukey's multiple comparison test).

(B) Frequency distribution of mitochondria-vesicle contacts with respect to the PM; the distance is normalized by cell size.

(C) Average distance from the PM after 25-mM glucose of stimulation (left) and 25-mM glucose + Ex-4 (right). No significance difference was seen in cells treated with glucose alone. A significant difference in the distance was observed after 5-min stimulation with glucose + Ex-4 with respect to 1 min (*p = 0.0453) and 30 min (*p = 0.0397) (Tukey's multiple comparison test). Error bars in panel (A) and (C) represent SDs.
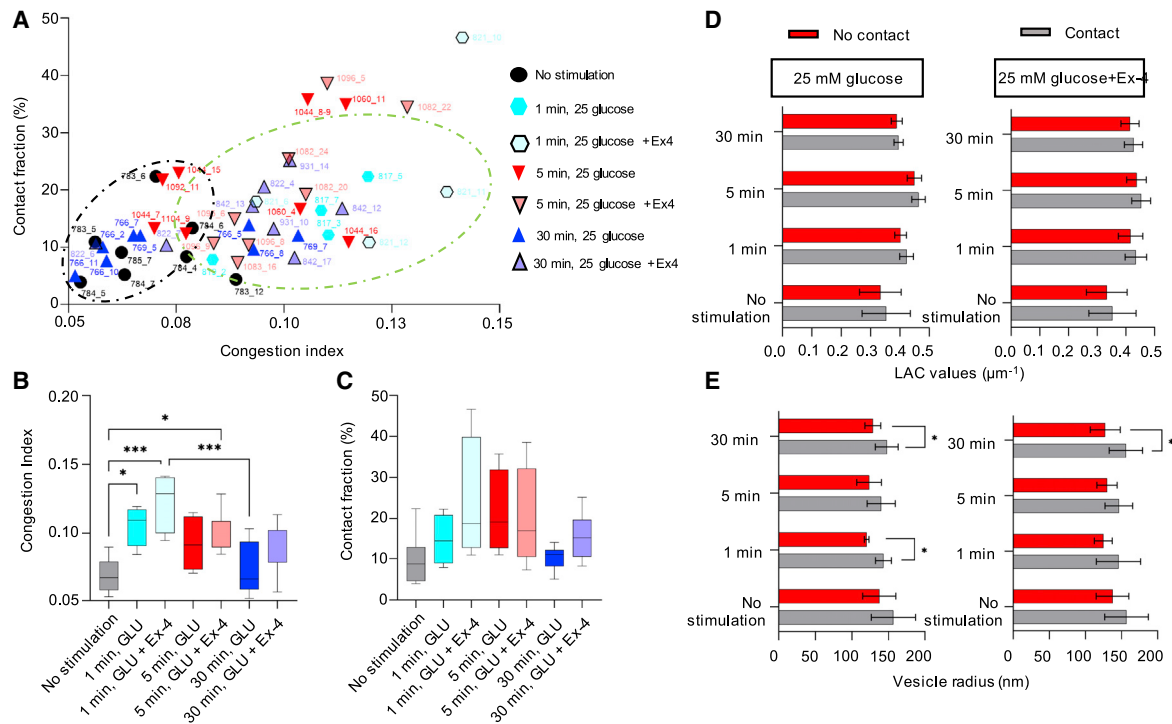
that the role of incretin in facilitating the mitochondrial biogenesis is dependent on glucose co-stimulation (Figure 6C). Like the treatment with high glucose + Ex-4, the LAC value of mitochondria is comparable between unstimulated cells (0.32 ± 0.02 μm^{-1}) and 5-min (0.32 ± 0.03 μm^{-1}) and 30-min Ex-4-stimulated cells (0.30 ± 0.03 μm^{-1}) (Figure 6D), confirming that the mitochondria molecular density is not altered by the treatment with Ex-4 alone. The distance between mitochondria and insulin vesicles is similarly affected by the treatment with Ex-4, inducing insulin vesicle and mitochondria association after 5 min of stimulation (Figure 6E). In terms of mitochondria-insulin vesicle interaction and contact distribution from the PM (Figures 6E–6F), Ex-4 treatment is less effective after 30 min of stimulation compared with after the high glucose + Ex-4 treatment (Figures 2C and 4). Finally, we correlated the C.I. for each cell with the fraction of insulin vesicles in contact with the mitochondrial network. Also in this case, we found that the increase of the mitochondria network volume is not directly correlated with the number of contacts per cell; after 30 min of treatment, we observe different numbers of contacts in the cells 1138_9, 1127_11, and 1141_9, but similar C.I.s (Figure 6G). Thus, we hypothesize that the vesicle-mitochondria association might be driven by cellular mechanisms that promote the enlargement of vesicle size (Figure 5E).

Finally, we conducted an ATP quantification assay to rationalize the relationship between mitochondria biogenesis and the effect of Ex-4. Although we observed an increase in the mitochondria volume after the stimulation with high glucose and Ex-4, we did not detect a significant difference in the amount of ATP produced within the first 30 min of stimulation with either high

glucose co-stimulation, but the direct effect of Ex-4 on the ultrastructural organization and chemical composition of cells has not been investigated. We verified the direct effect of Ex-4 on cell ultrastructure by decoupling drug and glucose stimulation and treating the cells with 10-nM Ex-4 alone for 5 and 30 min. Ex-4 alone does not increase the cumulative insulin vesicle volume, unlike what we observed after co-stimulation with glucose for 30 min (Table 1). Thus, Ex-4 stimulation alone does not drive insulin vesicle biogenesis. On the other hand, Ex-4 affects the chemical composition of the vesicles both after 5 and 30 min from the stimulation (Figure 6B), increasing the LAC values (untreated: 0.37 ± 0.03 μm^{-1}; 5 min: 0.44 ± 0.02 μm^{-1}; 30 min: 0.43 ± 0.04 μm^{-1}). Unlike the results shown in Figure 2A, Ex-4 increases the mitochondrial volume after 5 min, but this effect is not sustained during the second phase of secretion (30 min). Mitochondrial occupancy within the cell decreases during Ex-4 stimulation (unstimulated: 4.4% ± 0.9%; 5 min: 8.5% ± 3.4%; 30 min: 7.5% ± 2.0%), indicating

Figure 5. Analysis of the mitochondria-insulin vesicle interaction randomness

(A) The plot shows the correlation between the number of mitochondria-vesicle contacts and the congestion index (C.I.) per individual cell. The black circle shows clusters of cells with less crowding (lower C.I., 0.05–0.08) and percentage of contacts (3%–12%); the green circle shows those with more crowding (higher C.I., 0.08–0.14) and percentage of contacts (4%–25%) under different conditions.

(B) Mean value of the C.I. for each condition. Significant difference is reported between no stimulated cells and 1-min glucose-stimulated cells (*p = 0.0210), 1-min glucose- + Ex-4-stimulated cells (***p = 0.0002), and 5-min glucose- + Ex-4-stimulated cells (*p = 0.0153); a significant difference is also reported between 1-min glucose- + Ex-4-stimulated cells and 30-min glucose-stimulated cells (***p = 0.0007).

(C) Mean value of the faction of contacts per condition.

(D) Plot showing the LAC values of vesicles in contact (gray) and not in contact (red) with mitochondria, at each time point and stimulation, with no significant difference.

(E) Changes in the vesicle size whether in contact with the mitochondria network (gray) or not (red). The plot shows a significant difference between the size of vesicle after 1-min stimulation with glucose (143 ± 11 nm, contacts; 120 ± 3.0 nm, no contacts, *p = 0.0195) and 30-min stimulation with high glucose (148 ± 16 nm, contacts; 129 ± 11 nm, no contacts, *p = 0.0147) and high glucose + Ex-4 (155 ± 23 nm, contacts; 127 ± 21 nm, no contacts, *p = 0.0211). Error bars represent the SDs, and the statistical significance was evaluated using Welsh's test.

glucose or high glucose + Ex-4, and a lower level of ATP was measured within 30 min of stimulation with Ex-4 alone (Figure 6H). Thus, we hypothesize that despite the increase in the mitochondrial volume, the production of ATP was not enhanced by the treatment with Ex-4.

DISCUSSION

This study demonstrates the feasibility of quantifying rearrangements in the cellular ultrastructure at a high resolution (∼60 nm) using SXT. SXT can be used to quantify changes in organelle morphology and spatial distribution and to track the effects of cell stimulation over time. We detected rearrangements in mitochondria and insulin vesicle localization and their association during the first and second phases of the insulin secretion, consistent with previous observations reported in the literature (Maechler and Wollheim, 2001; White et al., 2020; Wollheim, 2000). Our data provide unprecedented insights into the cell-wide interactions between vesicles and mitochondria, showing

that most of the interactions during the first and second phases of secretion take place in close proximity to the PM, in agreement with the hypothesis that the interaction is functional for vesicle docking and fast release (Maechler and Wollheim, 2001). Similar evidence in the insulin vesicle radius variability in different cellular neighborhoods was observed by Zhang et al. (2020) who suggested that the interaction with mitochondria may contribute to the larger radius of vesicles localized in close proximity to the PM, where the interaction is more frequent. Future use of cryo-ET may help to capture the local mitochondria-insulin vesicle interaction; however, this would require correlation with fluorescence microscopy to target the sites of interaction. Ex-4 enhances the interaction of vesicles and mitochondria, contributing to a fast rearrangement of cellular ultrastructure. Ultrastructural rearrangements on this scale and at high resolutions are difficult to investigate using conventional microscopy since, for instance, the use of classical TEM reveals only local rearrangements in the cellular ultrastructure (Fava et al., 2012; Wollheim, 2000). More recently, developments of
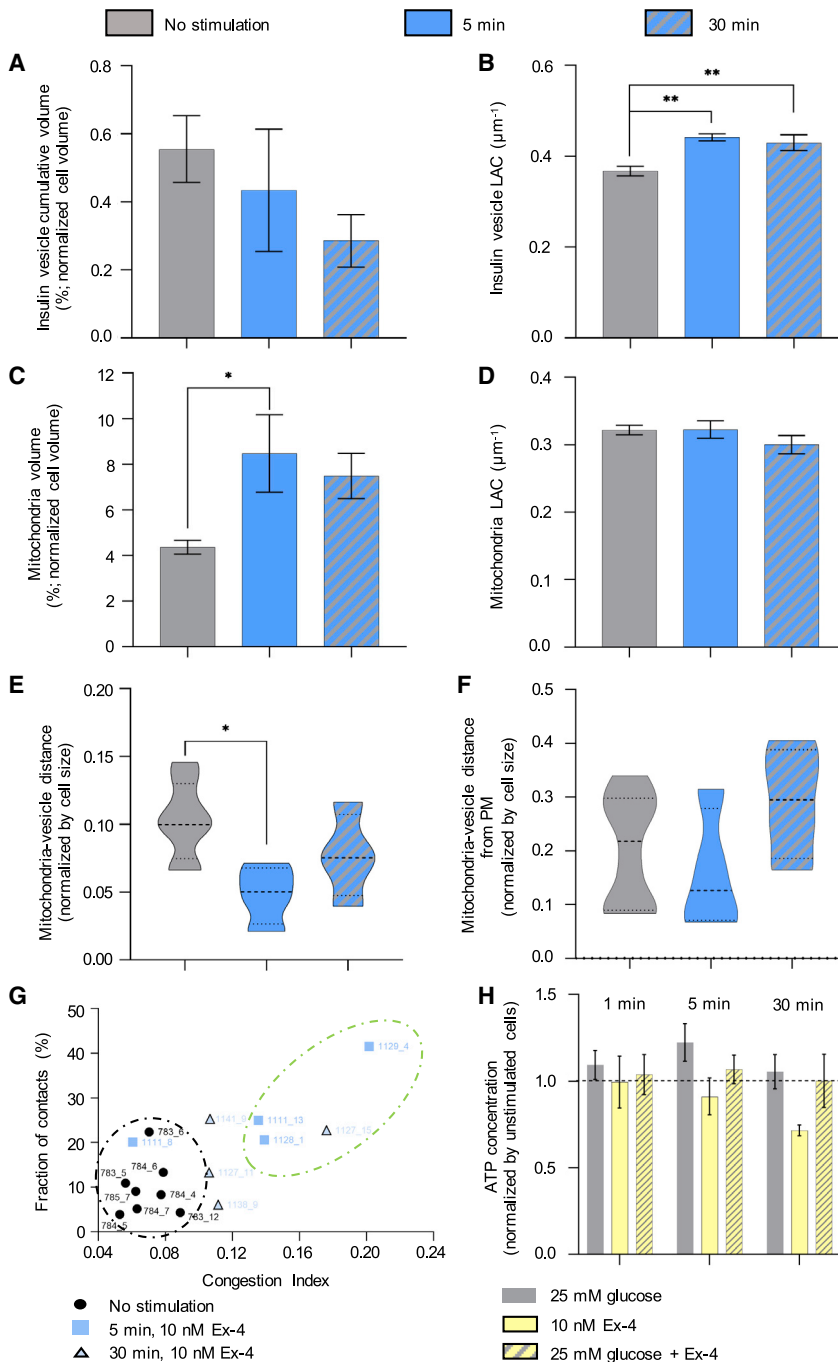
Figure 6. Effect of Ex-4 on the organelle properties

(A) Percentage of cell volume occupied by insulin vesicles in unstimulated, 5-min, and 30-min post stimulation with 10-nM Ex-4.

(B) LAC of insulin vesicles treated with Ex-4. Statistical significance was found between the unstimulated (0.37 ± 0.03 μm^{-1}) and 5-min (0.44 ± 0.02 μm^{-1}, **p = 0.0026) and 30-min (0.43 ± 0.04 μm^{-1}, **p = 0.0089) post stimulation.

(C) Percentage of cell volume occupied by the mitochondrial network. Statistical significance was observed after stimulating the cells for 5 min with Ex-4 ($8.5\% \pm 3.4\%$, *p = 0.0133) compared with unstimulated cells ($4.4\% \pm 0.9\%$).

(D) There were no significant differences in LAC values for mitochondria treated for 5 (0.32 ± 0.03 μm^{-1}) and 30 (0.30 ± 0.03 μm^{-1}) min with Ex-4 compared with untreated cells (0.32 ± 0.02 μm^{-1}).

(E) There was a significant difference in the mean distance between mitochondria and insulin vesicles in unstimulated cells and cells treated for 5 min (*p = 0.0166).

(F) There was no significant difference in mitochondria-vesicle contacts at different distances from the PM (normalized by cell size) between unstimulated cells and after 5 and 30 min of stimulation.

(G) Correlation between C.I. and fraction of vesicles in contact with mitochondria in unstimulated cells and cells after 5 and 30 min of stimulation with Ex-4. Two clusters are highlighted: the black circle shows cells with low C.I.s (0.04–0.08) and fractions of contacts; the green circle shows cells with high C.I.s (0.12–0.20) and high fractions of contacts (20%–42%).

(H) ATP concentration of cells treated with high glucose ± Ex-4 and Ex-4 alone. The ATP concentration for each condition is normalized by the ATP concentration in unstimulated cells. The black line shows the distance between the ATP value in the unstimulated cells and cells treated with glucose and Ex-4. In all panels, the statistical significance was evaluated using Tukey's multiple comparison test and error bars represent the SDs.

FIB-SEM have shown distinct interactions between insulin vesicles and microtubules in primary β cells, allowing for the quantification of the distribution of insulin vesicles in contact with microtubules from the nucleus and PM and for defining the role of the cytoskeleton in the process of vesicle transfer from the Golgi (Müller et al., 2020). Despite the high resolution achieved by electron microscopy over the past decade, the requirement of sample fixation, staining, dehydrating, and slicing adds time-consuming steps that limit the numbers of cells that can be investigated. However, the combination of electron micro-

scopy with SXT will be a valuable tool to identify the role of organelles not seen in SXT due to limitations of resolution and contrast (e.g., cytoskeleton) (Chichón et al., 2012).

A unique feature of SXT is the quantitative nature of the LAC value, which allows for the detection of alterations in the molecular density of subcellular compartments (McDermott et al., 2012). We observed a significant increase in the mitochondria LAC value after treating the cells for 5 min with 25-mM glucose, revealing the possible activation of mechanisms that involve the respiratory cycle and glucose metabolism (Maechler et al., 2006); on the contrary, we could not identify changes in the mitochondria LAC after treatment with only glucose or Ex-4 after 1 and 30 min of stimulation. Also, the average LAC values for cellular components in different stages allows us to locally track the effect of interactions between different organelles. In this

specific case, we did not observe a statistically significant variation in the LAC as a response to association of insulin vesicles with mitochondria; however, we could see an increase in vesicle size, as detected with mature vesicles in proximity to the PM (Suckale and Solimena, 2010; Zhang et al., 2020). Our study paves the way for the investigation of the metabolic and protein signaling processes that enhance the interaction between mitochondria and insulin vesicles to explore the dynamics of organelle cross-talk in the cell. We provide evidence for the spatial proximity of vesicles to mitochondria, suggesting possible inter-organelle communication. Similarly, such interaction is corroborated by the enlargement of the vesicles in contact with the mitochondrial network at different time points during the insulin secretion process. Altogether, these data can contribute to the design of live-cell, proteomic, and metabolomic experiments, focusing on the enrichment of vesicle and mitochondria components. Moreover, to further investigate the role of this interaction, the use of fluorescent probes targeting putative proteins involved in the interaction will provide an additional tool to explore the cell dynamics via live-cell or pulse-chase experiments, informed by the time points observed via SXT.

A shortfall of SXT imaging is the lack of details at the molecular level, which would inform about physical interactions among organelles. This lack of information is readily overcome by correlating SXT reconstructions with fluorescence data acquired from the same specimen. Individual molecules can be spatially localized based on the overlay of the fluorescence signal with the X-ray absorption (Smith et al., 2014). Moreover, the development of cryogenic fluorescence microscopes has significantly improved this multi-scale description of the cell (Elgass et al., 2015). For instance, the use of fluorescently labeled insulin vesicles will help in elucidating the role of vesicle maturation in association with mitochondria, confirming that the association may activate the maturation process. Moreover, our results will inform future live-cell imaging experiments by providing a general time-scale as well as the specific regions of the cell in which to observe vesicle-mitochondria contacts. Another limitation is the time-consuming segmentation process; the lack of an automatic pipeline for organelle identification and annotation increases the time to obtain a segmented 3D reconstruction for analysis. However, recent efforts in the development of machine-learning-based segmentation tools will facilitate the analysis and interpretation of whole-cell SXT data in a shorter time (Francis et al., 2020).

To conclude, SXT combines the short time of data collection (<10 min) with the quantitative description of subcellular features, opening the way to the spatiotemporal mapping of cell reorganization. This approach can, in fact, be applied to any organelle-organelle interaction within any cell type and can inform about intracellular systemic interactions with minimal cell manipulation. Therefore, SXT can be considered a very useful tool to augment data-driven models (Raveh et al., 2021; Singla et al., 2018; Singla and White, 2021) and to provide details about 3D subcellular reorganization in healthy and pathological conditions.

STAR★METHODS

Detailed methods are provided in the online version of this paper and include the following:

- KEY RESOURCE TABLE
- RESOURCE AVAILABILITY
  - Lead contact
  - Materials availability
  - Data and code availability
- EXPERIMENTAL MODEL AND SUBJECT DETAILS
- METHOD DETAILS
  - Cell stimulation
  - SXT sample preparation and data collection
  - ATP quantification assay
  - Segmentation and LAC quantification
  - Insulin vesicle distance from PM and mitochondria and vesicle-mitochondria contact distribution
  - Identification of LAC and size of insulin vesicles associated to mitochondria
  - Congestion index
- QUANTIFICATION AND STATISTICAL ANALYSIS

AUTHOR CONTRIBUTIONS

C.A.L., K.L.W., and V.L. designed the project. V.L and J.-H.C. prepared the samples and collected the X-ray data. V.L. and K.L.W. performed cell-culture stimulation and segmented the data. J.S. and A.L. provided the pipeline for the analysis of vesicle distance and the mitochondria-vesicle interactions. A.E. assisted with the analysis and reconstruction of the tomograms. G.M. helped with the interpretation and data segmentation. M.L.G. assisted with the data collection. C.A.L., K.L.W., and A.S. provided guidance with the analysis, interpretation, and discussion. V.L. wrote the manuscript with contributions from all co-authors.

DECLARATION OF INTERESTS

The authors declare no competing interests.

REFERENCES

Attwood, D.T. (2000). Soft X-Rays and Extreme Ultraviolet Radiation (Cambridge University Press).

Bratanova-Tochkova, T.K., Cheng, H., Daniel, S., Gunawardana, S., Liu, Y.-J., Mulvaney-Musa, J., Schermerhorn, T., Straub, S.G., Yajima, H., and Sharp, G.W.G. (2002). Triggering and augmentation mechanisms, granule pools, and biphasic insulin secretion. Diabetes 51, S83.

Buckley, G., Gervinskas, G., Taveneau, C., Venugopal, H., Whisstock, J.C., and de Marco, A. (2020). Automated cryo-lamella preparation for high-throughput in-situ structural biology. J. Struct. Biol 210, 107488. https://doi.org/10.1016/j.jsb.2020.107488.

Chichón, F.J., Rodríguez, M.J., Pereiro, E., Chiappi, M., Perdiguero, B., Guttmann, P., Werner, S., Rehbein, S., Schneider, G., Esteban, M., et al. (2012). Cryo X-ray nano-tomography of vaccinia virus infected cells. J. Struct. Biol. *177*, 202–211.

Cohen, S., Valm, A.M., and Lippincott-Schwartz, J. (2018a). Interacting organelles. Curr. Opin. Cell Biol. *53*, 84–91.

Cohen, S., Valm, A.M., and Lippincott-Schwartz, J. (2018b). Multispectral live-cell imaging. Curr. Protoc. Cell Biol. *79*, e46.

Díaz, P., Sandoval-Bórquez, A., Bravo-Sagua, R., Quest, A.F.G., and Lavandero, S. (2021). Perspectives on organelle interaction, protein dysregulation, and cancer disease. Front. Cell Developmental Biol. *9*, 613336.

Do, M., Isaacson, S.A., McDermott, G., Le Gros, M.A., and Larabell, C.A. (2015). Imaging and characterizing cells using tomography. Arch. Biochem. Biophys. *581*, 111–121.

Duke, E., Dent, K., Razi, M., and Collinson, L.M. (2014). Biological applications of cryo-soft X-ray tomography. J. Microsc. *255*, 65–70.

Ekman, A.A., Chen, J.H., Guo, J., McDermott, G., Le Gros, M.A., and Larabell, C.A. (2017). Mesoscale imaging with cryo-light and X-rays: larger than molecular machines, smaller than a cell. Biol. Cell *109*, 24–38.

Elgass, K.D., Smith, E.A., LeGros, M.A., Larabell, C.A., and Ryan, M.T. (2015). Analysis of ER-mitochondria contacts using correlative fluorescence microscopy and soft X-ray tomography of mammalian cells. J. Cell Sci *128*, 2795–2804.

Eng, J., Kleinman, W.A., Singh, L., Singh, G., and Raufman, J.P. (1992). Isolation and characterization of exendin-4, an exendin-3 analogue, from Heloderma suspectum venom. Further evidence for an exendin receptor on dispersed acini from Guinea pig pancreas. J. Biol. Chem. *267*, 7402–7405.

Fava, E., Dehghany, J., Ouwendijk, J., Müller, A., Niederlein, A., Verkade, P., Meyer-Hermann, M., and Solimena, M. (2012). Novel standards in the measurement of rat insulin granules combining electron microscopy, high-content image analysis and in silico modelling. Diabetologia *55*, 1013–1023.

Francis, J.P., Wang, H., White, K., Syeda-Mahmood, T., and Stevens, R. (2020). Neural network segmentation of cell ultrastructure using incomplete annotation. In 2020 IEEE 17th International Symposium on Biomedical Imaging (ISBI) (IEEE), pp. 1183–1187.

Gedulin, B.R., Nikoulina, S.E., Smith, P.A., Gedulin, G., Nielsen, L.L., Baron, A.D., Parkes, D.G., and Young, A.A. (2005). Exenatide (Exendin-4) improves insulin sensitivity and β-cell mass in insulin-resistant obese fa/fa zucker rats independent of glycemia and body weight. Endocrinology *146*, 2069–2076.

Graham, B.J., Hildebrand, D.G.C., Kuan, A.T., Maniates-Selvin, J.T., Thomas, L.A., Shanny, B.L., and Lee, W.C.A. (2019). High-throughput transmission electron microscopy with automated serial sectioning. bioRxiv, 657346.

Groen, J., Conesa, J.J., Valcárcel, R., and Pereiro, E. (2019). The cellular landscape by cryo soft X-ray tomography. Biophysical Rev. *11*, 611–619.

Guo, Y., Li, D., Zhang, S., Yang, Y., Liu, J.J., Wang, X., Liu, C., Milkie, D.E., Moore, R.P., Tulu, U.S., et al. (2018). Visualizing intracellular organelle and cytoskeletal interactions at nanoscale resolution on millisecond timescales. Cell *175*, 1430–1442.e1417.

Henne, W.M. (2021). Organelle homeostasis principles: how organelle quality control and inter-organelle crosstalk promote cell survival. Developmental Cell *56*, 878–880.

Kalavalapalli, S., Bril, F., Guingab, J., Vergara, A., Garrett, T.J., Sunny, N.E., and Cusi, K. (2019). Impact of exenatide on mitochondrial lipid metabolism in mice with nonalcoholic steatohepatitis. J. Endocrinol. *241*, 293–305.

Kang, M.Y., Oh, T.J., and Cho, Y.M. (2015). Glucagon-like peptide-1 increases mitochondrial biogenesis and function in INS-1 rat insulinoma cells. Endocrinol. Metab. *30*, 216–220.

Kizilyaprak, C., Bittermann, A.G., Daraspe, J., and Humbel, B.M. (2013). FIB-SEM tomography in biology. In Electron Microscopy Methods in Molecular Biology (Methods and Protocols) (Totowa, NJ): Humana Press), pp. 541–558.

Kolterman, O.G., Buse, J.B., Fineman, M.S., Gaines, E., Heintz, S., Bicsak, T.A., Taylor, K., Kim, D., Aisporna, M., Wang, Y., et al. (2003). Synthetic exendin-4 (Exenatide) significantly reduces postprandial and fasting plasma glucose in subjects with type 2 diabetes. J. Clin. Endocrinol. Metab. *88*, 3082–3089.

Kremer, A., Lippens, S., Bartunkova, S., Asselbergh, B., Blanpain, C., Fendrych, M., Goossens, A., Holt, M., Janssens, S., Krols, M., et al. (2015). Developing 3D SEM in a broad biological context. J. Microsc. *259*, 80–96.

Kremer, J.R., Mastronarde, D.N., and McIntosh, J.R. (1996). Computer visualization of three-dimensional image data using IMOD. J. Struct. Biol. *116*, 71–76.

Larabell, C.A., and Nugent, K.A. (2010). Imaging cellular architecture with X-rays. Curr. Opin. Struc Biol. *20*, 623–631.

Le Gros, M.A., Knoechel, C.G., Uchida, M., Parkinson, D.Y., McDermott, G., and Larabell, C.A. (2012). 2.6 Visualizing sub-cellular organization using soft X-ray tomography. In Comprehensive Biophysics, H.E. Edward, ed. (Amsterdam: Elsevier), pp. 90–110.

Le Gros, M.A., McDermott, G., Cinquin, B.P., Smith, E.A., Do, M., Chao, W.L., Naulleau, P.P., and Larabell, C.A. (2014). Biological soft X-ray tomography on beamline 2.1 at the advanced light source. J. Synchrotron Radiat. *21*, 1370–1377.

Le Gros, M.A., Clowney, E.J., Magklara, A., Yen, A., Markenscoff-Papadimitriou, E., Colquitt, B., Myllys, M., Kellis, M., Lomvardas, S., and Larabell, C.A. (2016). Soft X-Ray tomography reveals gradual chromatin compaction and reorganization during neurogenesis in vivo. Cell Rep. *17*, 2125–2136.

Loconte, V., Chen, J.-H., Cortese, M., Ekman, A., Le Gros, M.A., Larabell, C., Bartenschlager, R., and Weinhardt, V. (2021). Using soft X-ray tomography for rapid whole-cell quantitative imaging of SARS-CoV-2-infected cells. Cell Rep. Methods *1*, 100117.

Lučić, V., Rigort, A., and Baumeister, W. (2013). Cryo-electron tomography: the challenge of doing structural biology in situ. J. Cell Biol. *202*, 407–419.

Maechler, P., Carobbio, S., and Rubi, B. (2006). In beta-cells, mitochondria integrate and generate metabolic signals controlling insulin secretion. Int. J. Biochem. Cell Biol. *38*, 696–709.

Maechler, P., and Wollheim, C.B. (2001). Mitochondrial function in normal and diabetic β-cells. Nature *414*, 807–812.

Mahamid, J., Pfeffer, S., Schaffer, M., Villa, E., Danev, R., Cuellar, L.K., Förster, F., Hyman, A.A., Plitzko, J.M., and Baumeister, W. (2016). Visualizing the molecular sociology at the HeLa cell nuclear periphery. Science *351*, 969–972.

McDermott, G., Fox, D.M., Epperly, L., Wetzler, M., Barron, A.E., Le Gros, M.A., and Larabell, C.A. (2012). Visualizing and quantifying cell phenotype using soft X-ray tomography. BioEssays *34*, 320–327.

McDermott, G., Le Gros, M.A., Knoechel, C.G., Uchida, M., and Larabell, C.A. (2009). Soft X-ray tomography and cryogenic light microscopy: the cool combination in cellular imaging. Trends Cell Biol. *19*, 587–595.

Müller, A., Schmidt, D., Xu, C.S., Pang, S., D'Costa, J.V., Kretschmar, S., Münster, C., Kurth, T., Jug, F., Weigert, M., et al. (2020). 3D FIB-SEM reconstruction of microtubule–organelle interaction in whole primary mouse β cells. J. Cell Biol. *220*, e202010039.

Noske, A.B., Costin, A.J., Morgan, G.P., and Marsh, B.J. (2008). Expedited approaches to whole cell electron tomography and organelle mark-up in situ in high-pressure frozen pancreatic islets. J. Struct. Biol. *161*, 298–313.

Parkinson, D.Y., Epperly, L.R., McDermott, G., Le Gros, M.A., Boudreau, R.M., and Larabell, C.A. (2013). Nanoimaging cells using soft X-ray tomography. Methods Mol. Biol. *950*, 457–481.

Parkinson, D.Y., Knoechel, C., Yang, C., Larabell, C.A., and Le Gros, M.A. (2012). Automatic alignment and reconstruction of images for soft X-ray tomography. J. Struct. Biol. *177*, 259–266.

Peet, M.J., Henderson, R., and Russo, C.J. (2019). The energy dependence of contrast and damage in electron cryomicroscopy of biological molecules. Ultramicroscopy *203*, 125–131.

Phillips, M.J., and Voeltz, G.K. (2016). Structure and function of ER membrane contact sites with other organelles. Nat. Rev. Mol. Cell Biol. *17*, 69–82.

Raveh, B., Sun, L., White, K.L., Sanyal, T., Tempkin, J., Zheng, D., Bharat, K., Singla, J., Wang, C., Zhao, J., et al. (2021). Bayesian metamodeling of complex

biological systems across varying representations. Proc Natl Acad Sci U S A *118*. e2104559118. https://doi.org/10.1073/pnas.2104559118.

Rorsman, P., Eliasson, L., Renström, E., Gromada, J., Barg, S., and Göpel, S. (2000). The cell physiology of biphasic insulin secretion. Physiology *15*, 72–77.

Schneider, G., Guttmann, P., Heim, S., Rehbein, S., Mueller, F., Nagashima, K., Heymann, J.B., Müller, W.G., and McNally, J.G. (2010). Three-dimensional cellular ultrastructure resolved by X-ray microscopy. Nat. Methods *7*, 985–987.

Schindelin, J., Arganda-Carreras, I., Frise, E., Kaynig, V., Longair, M., Pietzsch, T., Preibisch, S., Rueden, C., Saalfeld, S., Schmid, B., et al. (2012). Fiji: an open-source platform for biological-image analysis. Nat. Methods *9*, 676–682.

Scorrano, L., De Matteis, M.A., Emr, S., Giordano, F., Hajnóczky, G., Kornmann, B., Lackner, L.L., Levine, T.P., Pellegrini, L., Reinisch, K., et al. (2019). Coming together to define membrane contact sites. Nat. Commun. *10*, 1287.

Singla, J., McClary, K.M., White, K.L., Alber, F., Sali, A., and Stevens, R.C. (2018). Opportunities and challenges in building a spatiotemporal multi-scale model of the human pancreatic β cell. Cell *173*, 11–19.

Singla, J., and White, K.L. (2021). A community approach to whole-cell modeling. Curr. Opin. Syst. Biol. *26*, 33–38.

Smith, E.A., McDermott, G., Do, M., Leung, K., Panning, B., Le Gros, M.A., and Larabell, C.A. (2014). Quantitatively imaging chromosomes by correlated cryo-fluorescence and soft x-ray tomographies. Biophysical J. *107*, 1988–1996.

Suckale, J., and Solimena, M. (2010). The insulin secretory granule as a signaling hub. Trends Endocrinol. Metab. *21*, 599–609.

Valm, A.M., Cohen, S., Legant, W.R., Melunis, J., Hershberg, U., Wait, E., Cohen, A.R., Davidson, M.W., Betzig, E., and Lippincott-Schwartz, J. (2017). Applying systems-level spectral imaging and analysis to reveal the organelle interactome. Nature *546*, 162–167.

Vance, J.E. (2014). MAM (mitochondria-associated membranes) in mammalian cells: lipids and beyond. Biochim. Biophys. Acta (Bba) - Mol. Cell Biol. Lipids *1841*, 595–609.

Weinhardt, V., Chen, J.H., Ekman, A.A., Guo, J., Remesh, S.G., Hammel, M., McDermott, G., Chao, W., Oh, S., Gros, M.A.L., et al. (2020). Switchable resolution in soft x-ray tomography of single cells. PLoS ONE *15*, 1–14.

White, K.L., Singla, J., Loconte, V., Chen, J.H., Ekman, A., Sun, L., Zhang, X., Francis, J.P., Li, A., Lin, W., et al. (2020). Visualizing subcellular rearrangements in intact β cells using soft x-ray tomography. Sci. Adv. *6*, 1–13.

Wiederkehr, A., and Wollheim, C.B. (2006). Minireview: implication of mitochondria in insulin secretion and action. Endocrinology *147*, 2643–2649.

Wollheim, C.B. (2000). Beta-cell mitochondria in the regulation of insulin secretion: a new culprit in type II diabetes. Diabetologia *43*, 265–277.

Zhang, X., Carter, S.D., Singla, J., White, K.L., Butler, P.C., Stevens, R.C., and Jensen, G.J. (2020). Visualizing insulin vesicle neighborhoods in β cells by cryo-electron tomography. Sci. Adv. *6*, eabc8258.

STAR★METHODS

KEY RESOURCE TABLE

REAGENT or RESOURCE	SOURCE	IDENTIFIER
Chemicals, Peptides and Recombinant proteins		
Addex Bio Optimized RPMI media	Addex Bio	Cat# C0004-02
Heat inactivated FBS	Fisher Scientific	Cat# 35-011-CV
PBS	Thermo Scientific	Cat# 10010023
1xPen/Strep	Invitrogen	Cat# 15140-148
β-mercaptoethanol	Invitrogen	Cat# 21985-023
Glucose	Sigma	Cat# 67021
NaCl	Sigma	Cat# S9888
NaHCO$_3$	Sigma	Cat# S5761
KCl	Sigma	Cat# 746436
MgCl$_2$	Sigma	Cat# M2670
CaCl$_2$ x 2H$_2$O	Sigma	Cat# C7902
BSA	Sigma	Cat# A3912
HEPES	Sigma	Cat#H4034
Exendin-4	Med Chem Express	Cat# HY-13443
Critical Commercial Assays		
Luminescent ATP Detection Assay Kit	Abcam	Cat# Ab113849
Deposited Data		
Raw and analyzed data (no stimulated cells, 5 min and 30 min 25 mM glucose stimulated cells and 25 mM glucose + Ex-4 stimulated cells)	(White et al., 2020)	N/A
Raw and analyzed data (1 min 25 mM glucose stimulated cells and 25 mM glucose + Ex-4 stimulated cells; 5 min and 30 min 10 nM Ex-4 stimulated cells)	This paper	N/A
Experimental Models: Cell Lines		
INS-1E	Addex Bio	Cat# C0018009; RRID: CVCL_0351
Software and Algorithms		
ImageJ – Fiji 1.53 c	(Schindelin et al., 2012)	https://imagej.nih.gov/ij/
GraphPad Prism 9.2	GraphPad	https://www.graphpad.com/scientific-software/prism/
Amira 2019.1	Thermo Scientific	https://thermofisher.com/amira-avizo
IMOD – 4.10.42	(Kremer et al., 1996)	https://bio3d.colorado.edu/imod/
AREC reconstruction	(Parkinson et al., 2012)	N/A
Organelle distribution pipeline	(White et al., 2020)	N/A
Contact distribution pipeline	This paper	N/A
Identification of LAC and size of insulin vesicles associated to mitochondria	This paper	N/A

RESOURCE AVAILABILITY

Lead contact
Further information and requests for resources and reagents could be addressed to and fulfilled by the lead contact: Carolyn A. Larabell (carolyn.larabell@ucsf.edu).

Materials availability
This study did not generate new reagents.

Data and code availability
All original code and reconstructed data are available from the corresponding contacts upon request.

Any additional information required to reanalyze the data reported in this paper is available from the corresponding contacts upon request.

EXPERIMENTAL MODEL AND SUBJECT DETAILS

Cell line: Rat insulinoma INS-1E cell line was obtained from ATCC. Cells were cultured in T75 flasks with Optimized RPMI media supplemented with 10% FBS, 1× Pen/Strep, and 0.05 mM β-mercaptoethanol and seeded at a density of 4.0×10^5 cells/cm^2. All cells were grown at 37°C, in a 5% CO_2 atmosphere.

METHOD DETAILS

Cell stimulation
Before glucose treatment, the cells were incubated in 4 mL of Krebs-Ringer bicarbonate buffer (KREBs) (115 mM NaCl, 24 mM $NaHCO_3$, 5 mM KCl, 1 mM $MgCl_2$, and 1 mM $CaCl_2$) supplemented with 10 mM Hepes (pH 7.4), 0.1% bovine serum albumin, and 1.1 mM glucose for 30 min at 37°C. The glucose starvation buffer was then removed and replaced with 2 mL of buffer containing either 25 mM glucose, 25 mM glucose+10 nM Ex-4, or 10 nM Ex-4 and incubated for 1, 5, or 30 min at 37°C, in 5% CO_2 atmosphere.

SXT sample preparation and data collection
Cells were removed from the T75 flask and treated in suspension as reported in the previous paragraph. Cell were harvested by centrifugation at 300g for 6 min, resuspended in Krebs buffer, and loaded in thin-walled glass capillaries (1.5 μL per loading). Each capillary was then rapidly plunged-frozen in nitrogen-cooled liquid propane (Parkinson et al., 2013).

Projection images were collected at 517 eV using XM-2 (Le Gros et al., 2014), the National Center for X-ray Tomography soft X-ray microscope at the Advanced Light Source of Lawrence Berkeley National Laboratory; the microscope was equipped with a 60-nm resolution objective lens. During data collection, cells were maintained in a stream of helium gas cooled to liquid nitrogen temperatures (Parkinson et al., 2013), which allows the collection of projection images while reducing the effects of exposure to radiation. Projection images were collected sequentially around a rotation axis of 180°, with 2° increments. Depending on the synchrotron ring current, an exposure time of 140 and 350 ms was used. The image 3D reconstruction was achieved using an iterative reconstruction method in the software package AREC3D (Parkinson et al., 2012). For comparison, all data were normalized and transferred to linear absorption coefficient by accounting for pixel size.

ATP quantification assay
Cell ATP level was measured from cells grown in a 96-well plate, with 4 repeats for each condition. Cells were treated with 25 mM glucose, 25 mM glucose + Ex-4, and Ex-4 alone. The experiment was performed on unstimulated cells and cells stimulated for 1, 5, and 30 min 50 μL of detergent (ATP luminescence detection kit, Abcam, ab113849) were added to each well to lyse the cells and stabilize the ATP, followed by 50 μL of substrate. Cell lysate was then incubated in the dark for 15 min. Luminescence was read for 2s using a plate reader. Substrate solution was used as blank.

Segmentation and LAC quantification
All cells were manually segmented using the software Amira 2019.1 (Thermo Scientific™). The identification of each type of organelles was based on previously published data (McDermott et al., 2009; White et al., 2020). The nucleus was manually segmented at first in every 10 ortho slices; each orthoslice was consequently interpolated to reconstruct the 3D label field. Mitochondria, lipid droplets, and insulin vesicles were both manually and semi-automatically segmented, setting the threshold of X-ray absorption to values reported in literature (McDermott et al., 2009; White et al., 2020). Lipid droplets were identified setting the threshold between 0.48 and 0.90 μm^{-1}, with maximum peak per droplet set at about 0.66 μm^{-1}. An average insulin vesicle LAC of 0.42 ± 0.03^{-1} μm was used to label these organelles with a range of LAC values that spans from 0.28 to 0.62 μm^{-1} was used along with morphology and size.

Insulin vesicle distance from PM and mitochondria and vesicle-mitochondria contact distribution

The distance of each insulin vesicle from the PM and mitochondria was calculated using Euclidean distance transform (EDT). For distribution from the PM, the shortest distance between the vesicle center and the PM was considered, and for the distribution of the vesicles from the mitochondria we considered the shortest distance between vesicle center and the mitochondria mask. To also account for the change in the cell size across all conditions, the observed vesicle distance from both PM and mitochondria was normalized by the maximum EDT distance of the respective cell. The insulin vesicle-mitochondria contact-point distribution was generated applying the same strategy to the vesicle-mitochondria contact.

Identification of LAC and size of insulin vesicles associated to mitochondria

In each cell, the vesicle was considered in contact with mitochondria if the shortest distance between the vesicle surface and mitochondria mask was less than 1.5 voxels. The shortest distance was computed using EDT, similar to the distance of insulin vesicles from PM. Finally, the LAC and the volume of vesicles in contact or not in contact with the mitochondria network were extracted for each single instance. The mean values for each group were compared for each condition.

Congestion index

The congestion index (C.I.) describes the crowdedness of a single cell under a well-defined treatment and is defined as:

$$C.I. = \frac{V_{insulin} + V_{mitochondria}}{V_{cell} - V_{nucleus}}$$

where, $V_{insulin}$, $V_{mitochondria}$, V_{cell} and $V_{nucleus}$ are the insulin vesicles, mitochondria, whole cell and nucleus volume in the single cell, respectively. The index identifies the fraction of the non-nuclear volume in the cell occupied by insulin vesicles and mitochondria. The higher value of the C.I. corresponds to the crowded ultrastructure in the cell.

QUANTIFICATION AND STATISTICAL ANALYSIS

Data statistical analysis was performed using Prism (version 9.2, GraphPad Software, La Jolla, CA). The analysis of variance test (ANOVA) was used to determine statistical difference in the mean of three or more data populations. Each test was followed up by a *post hoc* test, reported in the main body of the text for each analysis. Welsh's test was used to determine statistical difference between the mean values of the LAC and the radius of insulin vesicles in contact and not in contact with mitochondria.